

Article

Finding the Limits of Magnetic Hyperthermia on Core-Shell Nanoparticles Fabricated by Physical Vapor Methods

Carlos Martinez-Boubeta ^{1,*}, Konstantinos Simeonidis ¹, Judit Oró ², Antonios Makridis ^{3,4}, David Serantes ⁵
and Lluís Balcells ²

¹ Ecoresources P.C., Giannitson-Santaroza 15-17, 54627 Thessaloniki, Greece; simeonidis@ecoresources.gr

² Institut de Ciència de Materials de Barcelona, CSIC, 08193 Bellaterra, Spain; oro@icmab.es (J.O.); balcells@icmab.es (L.B.)

³ Department of Physics, Aristotle University of Thessaloniki, 54124 Thessaloniki, Greece; anmakrid@physics.auth.gr

⁴ Laboratory of Magnetic Nanostructure Characterization, Technology and Applications (MagnaCharta), CIRI-AUTH, 57001 Thessaloniki, Greece

⁵ Applied Physics Department and Instituto de Investigaciones Tecnológicas, Universidade de Santiago de Compostela, 15782, Santiago de Compostela, Spain; david.serantes@usc.es

* Correspondence: cboubeta@gmail.com

Abstract: Magnetic nanoparticles can generate heat when exposed to an alternating magnetic field. Their heating efficacy is governed by their magnetic properties that are in turn determined by their composition, size and morphology. Thus far, iron oxides (e.g., magnetite, Fe₃O₄) have been the most popular materials in use, though recently bimagnetic core-shell structures are gaining ground. Herein we present a study on the effect of particle morphology on heating efficiency. More specifically, we use zero waste impact methods for the synthesis of metal/metal oxide Fe/Fe₃O₄ nanoparticles in both spherical and cubic shapes, which present an interesting venue for understanding how spin coupling across interfaces and also finite size effects may influence the magnetic response. We show that these particles can generate sufficient heat (hundreds of watts per gram) to drive hyperthermia applications, whereas faceted nanoparticles demonstrate superior heating capabilities than spherical nanoparticles of similar size.

Keywords: magnetic nanoparticles; core-shell; spin-coupling; physical vapor deposition; sustainable synthesis techniques; hyperthermia



Citation: Martinez-Boubeta, C.; Simeonidis, K.; Oró, J.; Makridis, A.; Serantes, D.; Balcells, L. Finding the Limits of Magnetic Hyperthermia on Core-Shell Nanoparticles Fabricated by Physical Vapor Methods.

Magnetochemistry **2021**, *7*, 49. <https://doi.org/10.3390/magnetochemistry7040049>

Academic Editor: Andrea Caneschi

Received: 13 March 2021

Accepted: 31 March 2021

Published: 2 April 2021

Publisher's Note: MDPI stays neutral with regard to jurisdictional claims in published maps and institutional affiliations.



Copyright: © 2021 by the authors. Licensee MDPI, Basel, Switzerland. This article is an open access article distributed under the terms and conditions of the Creative Commons Attribution (CC BY) license (<https://creativecommons.org/licenses/by/4.0/>).

1. Introduction

Thermal medicine is supposed to date back at least to the first millennium BC, when Herodotus (4.75) described the joy and healing that the Scythians experienced from hemp-laden whole-body steam baths. Since then, several heating techniques have been developed, for instance by means of radiofrequency antennas and ultrasounds. A major drawback of these protocols is the fact that they dissipate too much power into body tissues, limiting their clinical application. Therefore, there has been a growing interest in the possibility of locating magnetically controlled thermal energy to maximize the therapeutic effect at appropriate depths in the body while minimizing unwanted heating side effects [1]. Within this context, in 1957, the use of nanometer magnetic heating seeds (between 20 to 100 nm in size) to treat cancer was first proposed [2]. Nowadays, high frequency heating of magnetic nanoparticles (NPs), systems with units lying in the dimension range where magnetic nanoscale effects different than the bulk state are observed, is an incipient technique for many diverse applications ranging from the ablative treatment of some types of cancer to the curing of epoxy resins.

Most of its potential lies in the fact that the degree of order in the system changes in response to external magnetic stimuli; this is usually a hysteretic irreversible process, which increases the entropy, and hence causes the unavoidable heat dissipation. Heat

originates as a result of the work done by the magnetic field applied on the NPs, which can either cause them to rotate (extraparticle Brownian displacements), or to switch their magnetization (intraparticle Néel relaxation). The whole process that takes place releasing heat depends on the field parameters (frequency and intensity), the properties of the NPs (composition, size, shape), as well as the characteristics (viscosity) of the dispersion matrix. All these factors drive the magnetization process (a relevant review is available at [3]). For example, iron oxide NPs at concentrations of 5 mg per one gram of lymphoid tissue showed about 1.2 MHz as the optimum frequency when field intensities in the range up to about 25 kA/m were applied [2].

From there on, researchers have focused on optimizing chemical synthesis routes to adjust the composition, volume (V), and shape of the NPs, aiming to tune both their saturation magnetization (M_S), and effective anisotropy energy density constant (K_{eff}). Depending on the available fields, the specific loss power (SLP) of the system, a proxy for the heating efficiency of NPs, could be significantly enhanced by employing highly crystalline building blocks of 3d transition metals [4]. Unfortunately, those metals suffer from degradation and biocompatibility issues. Hence, an alternative option is using iron oxide core-shell nanostructures: not only because of the good biocompatibility of iron-oxides [5] but also because the core-shell structure allows for a fine tuning of the magnetic (and thus hyperthermia) properties [6]. In this regard, physical methods represent an advance with minimum use of chemical reagents in the development of nanotechnology [7].

The aim of this study is to illustrate the different effect of the shape tuning of core-shell Fe/Fe₃O₄ nanoparticles on their heating efficiency under high-frequency alternating magnetic fields. For this purpose, reference spherical and cubic NPs of comparable total and shell dimensions were produced by physical vapor deposition, a chemistry-free technique. Apart from the induced magnetic effects, iron oxide coating promotes the biocompatibility aspect of these systems in terms of the cancer treatment applications. The heating efficiency of their aqueous dispersions was evaluated under various magnetic hyperthermia conditions. The results were then compared to the theoretically estimated maximum achievable efficiency within the given field conditions, in order to interpret the severe limitations revealed during experimental practice.

2. Results

In this study, we utilized two different methods to produce core-shell Fe/Fe₃O₄ NPs: spherical nanocrystals were synthesized by concentrated solar-based medium-vacuum evaporation; those with cubic geometry were fabricated using a sputtering-based high-vacuum cluster gun.

2.1. Structure and Morphology

XRD diagrams of the two types of samples are shown in Figure 1. As illustrated, both systems are composed of metal iron and an iron oxide with inverse spinel structure, i.e., Fe₃O₄. The intensity of the identified peaks corresponding to each phase is in accordance with the core-shell configuration derived through TEM observations (Figure 2). In particular, spherical NPs have an average diameter of around 35 nm with relatively high polydispersity (~20%). The size distribution is shown in the Supplementary Material. A low-contrast layer that surrounds most of the particles (around 2.5 nm in thickness) is in agreement with the presence of the assumed iron core-iron oxide shell morphology. This oxide shell engulfing the metallic Fe core is polycrystalline.

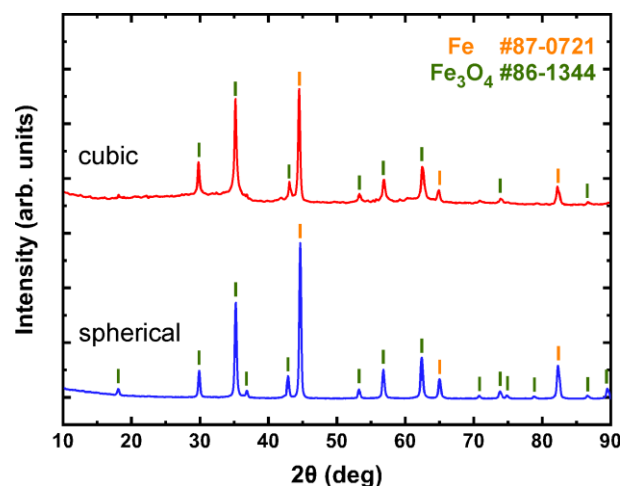


Figure 1. X-ray diffraction diagram of spherical and cubic core-shell Fe/Fe₃O₄ nanoparticles. Small lines indicate the corresponding peaks identified as Fe₃O₄ and Fe according to the JCPDS-PDF database cards #86-1344 and 87-0721, respectively.

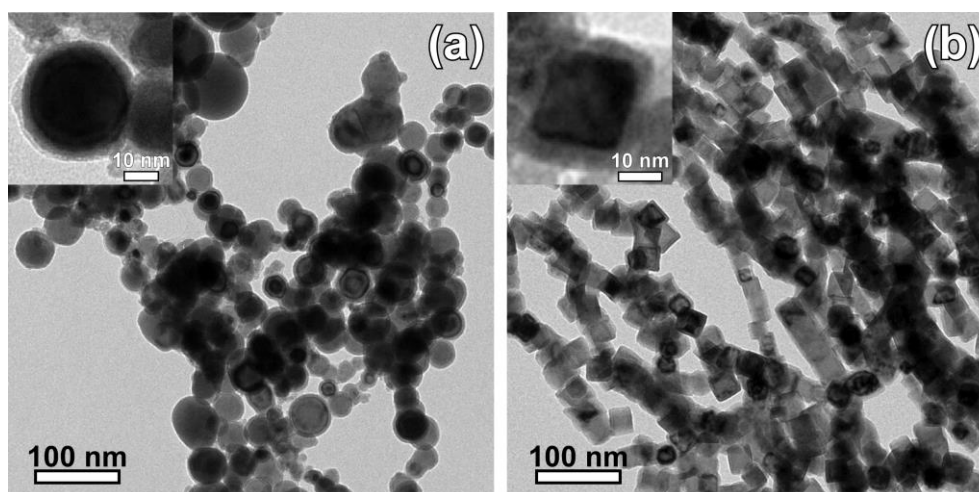


Figure 2. TEM images of (a) spherical and (b) cubic core-shell Fe/Fe₃O₄ nanoparticles showing the size distribution and the self-arrangement after evaporation of the solvent. Insets indicate detailed characteristics of the core and shell regions in magnified nanoparticles.

Cubic NPs present similar volume per particle (edge 27 nm) but improved monodispersity with a standard deviation 7.7%. The shell thickness is around 3 nm. Another important characteristic of nanocuboids is their broader tendency to self-assemble into long-range mesoscopic chains, with the presence of the flat surface facilitating the stability of such an arrangement in comparison to the spherical particles [8]. Such an effect, which is enhanced upon the drying of the dispersion, explains the higher aggregation rate of cubic nanoparticles giving the impression of a larger concentration in TEM images (Figure 2b). It should be mentioned that functionalization tests using aqueous-compatible ligands with affinity to the iron oxide caused only a slight modification of the nanoparticles' stability and distribution, which is explained by the relatively large size of the nanoparticles and the already good stability of the pure nanoparticles.

2.2. Magnetism and Heating Efficiency

The magnetic behavior of the two samples was assessed by recording the corresponding quasistatic hysteresis loops (Figure 3). The measurements were carried out in the field range above the saturation point, and at one of the fields (24 kA/m) tested during the

hyperthermia experiments. The saturation magnetization of spherical NPs approaches $150 \text{ Am}^2/\text{kg}$, which is indicative of a comparable presence of Fe and its oxides, while cubic NPs present a higher impact from the enriched oxide phase that shifts magnetization to lower values. The coercivity values for the two samples were found around 23.3 and 23.6 kA/m , respectively, for the spherical and cubic nanoparticles. For the specific particles size range where hysteresis losses represent the dominant magnetic heating mechanism, the evaluation of DC minor loops, at least qualitatively, appears as a reliable way to compare the heating potential of each sample [9]. In spite of the significant difference in M_S , minor loops at $\pm 24 \text{ kA/m}$ suggest that cubic NPs provide a higher energy product (i.e., hysteresis area) than spherical ones. Such property is reflected in the heating efficiency determined by calorimetric measurements under high-frequency fields. The recorded temperature versus time curves for heating (field-on) and cooling (field-off) conditions are shown in Figure 4 for different field intensities in the range 24–48 kA/m . By these diagrams it was possible to calculate SLP values after subtracting the coil heat contribution and the losses to the environment. The results are summarized in Table 1. For all conditions, the heating efficiency for cubic NPs is higher by at least 30%. This should be put in perspective with the 20% SLP enhancement for pure iron oxide NPs of similar sizes and shapes [10]. Notably, the analyses were repeated daily in the same dispersion over a timespan of one week without appreciable degradation, whereas the NPs powder showed the same magnetic behavior when checked for a period of 10 months after preparation.

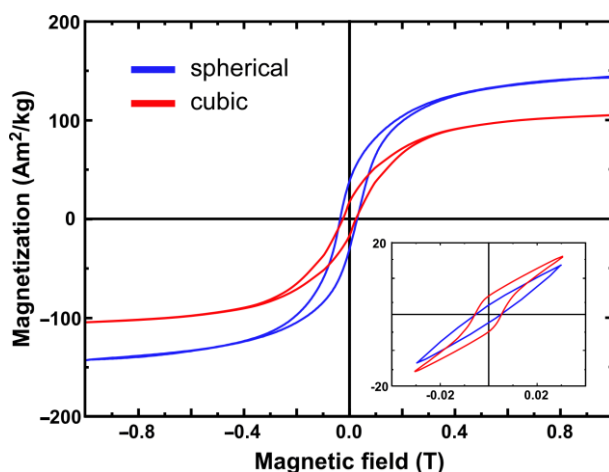


Figure 3. Magnetic hysteresis loops of studied samples at 300 K, and corresponding minor loop at maximum field of 24 kA/m shown in the inset.

Table 1. Specific loss power calorimetrically estimated for spherical and cubic core-shell $\text{Fe}/\text{Fe}_3\text{O}_4$ NPs.

AC Field (kA/m)	Specific Loss Power (W/g)	
	Spherical	Cubic
24	62 (± 4)	83 (± 4)
40	156 (± 8)	292 (± 11)
48	278 (± 12)	374 (± 13)

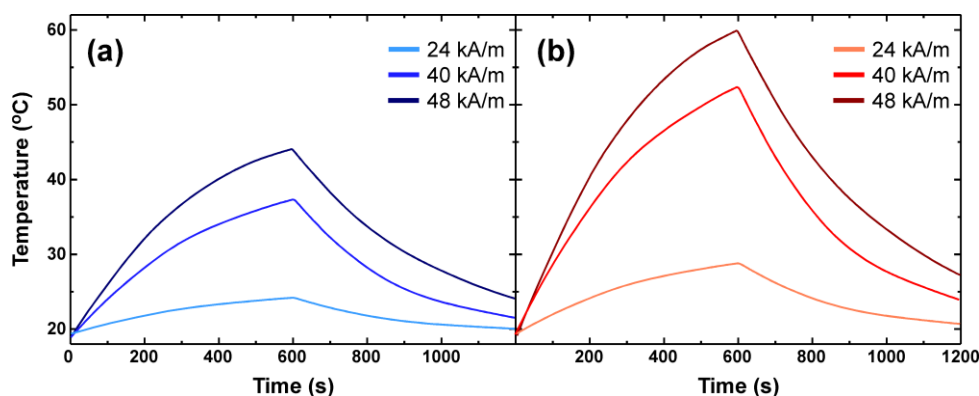


Figure 4. Temperature versus time heating and cooling curves for (a) spherical and (b) cubic core-shell Fe/Fe₃O₄ nanoparticles, obtained for 1 mg/mL water suspensions at applied AC field frequency 375 kHz and intensities 24–48 kA/m. Heating occurs for 600 s when the AC field is turned off.

3. Discussion

Magnetic NPs provide an ideal biomedical tool in cancer therapy, remotely controlled drug release and noninvasive magnetogenetics, thanks to their thermal losses during the electromagnetic cycling. However, there is a lack of understanding of the mechanisms responsible for this transfer of heat in the nanoscale. For instance, contrary to popular belief, high heating efficiency can only be achieved through hysteresis losses in large NPs (≥ 20 nm) systems, as it significantly exceeds that predicted by the linear superparamagnetic theory (defined as nonremanent quasistatic states at room temperature wherein the thermal fluctuations $k_B T$ dominate the magnetocrystalline anisotropy K_{eff}) [11,12]. At the same time, one can expect that the effect of the magnetostatic interactions on the hysteresis loop may boost the heat output [4,10,13,14].

3.1. Effect of Geometry

It is even more important that, as shown in the inset of Figure 3, the shape and area of the hysteresis loops for these nanoparticles differ considerably due to their different geometry. A parallelogram-shaped hysteresis is obtained in the case of the nanocubes, being quite different to the ellipsoidal-shape of the nanospheres. Thus, it can be assumed that the particles' geometry provides a simple mechanism for designing the K_{eff} of nanomagnets [10], though the contribution of the linear arrangement in cubic NPs and the higher standard deviation of spherical NPs should be also considered. However, the character of the magnetization curves depends also on the angular distribution of “easy axes” with respect to the field [14]. While the direction of the anisotropy easy axes of the spherical particles seems to be distributed at random, the near-perfect parallelogram shape for the minor hysteresis loop of the nanocubes sample indicates that their magnetization switches between two opposite directions along an easy axis, which is reasonable, given the increasing tendency of NPs to arrange in chains by sharing flat surfaces. Indeed, it resembles the coupling of vertically spaced vortex pairs [15], with parallel core polarizations and opposite helicity [16]. Recent work by some of us adds strong evidence that these cubes are in vortex states [17]. According to ref. [18], the effective single-domain size in cubes is smaller than that of spherical NPs, and it stems from the fact that the only bodies which can be uniformly magnetized are the ones bounded by quadric surfaces, particularly spheres [19]. Furthermore, polydispersity in particle size [20], or in the anisotropy energy per unit volume due to the different geometries of the samples [21], can also influence the measured performance. All the above-mentioned factors can explain the observed heating experiments (Figure 4).

However, the quantification of the several different parameters and the corresponding micromagnetic simulations of these nanostructures is beyond the scope of this paper. Still,

this issue may be briefly exemplified through the Stoner–Wohlfarth model. Figure 5 shows data that quantify performance achieved by core-shell NPs with similar composition to the studied ones in comparison to single-phase Fe_3O_4 NPs, the most commonly used material in hyperthermia studies. The comparison indicates that chain formation of cubic NPs enhances SLP values since it brings this system closer to the parameters of the ideal case. It can be assumed that if the cubic NPs showed similar randomness to the spherical ones, then their SLP results would be slightly lower than the corresponding ones for the spheres.

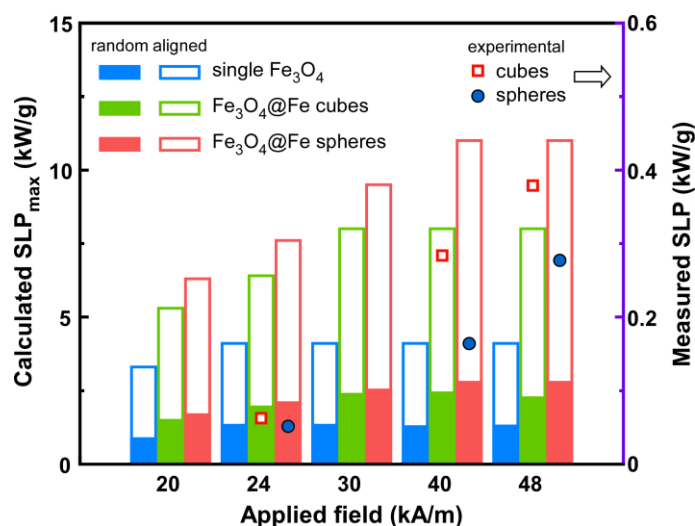


Figure 5. Estimation of the magnetic heating limit as function of the field strength at 375 kHz, for an “ideal” system of identical spherical or cubic-shaped $\text{Fe}_3\text{O}_4@Fe$ nanoparticles with characteristics similar to the studied ones, in comparison to single magnetite particles, with easy axes aligned in the field direction (empty bars) or randomly oriented (solid bars). Squares and circles indicate the experimentally determined values for spherical or cubic-nanoparticles corresponding to right y -axis. Please note the differences in axes scale.

3.2. Comparison with Other Core-Shell Systems

Numerically, the calculated SLP_{max} values for the situation of complete alignment of particles’ easy axes are much higher than our experimental ones, as is generally the case when comparing theory with experiment. In this light, studies reporting core-shell ferrites with heating efficiencies above 10 kW/g [22–24], would come close to the SLP_{max} values in Figure 5. There, the 10-fold improvement over conventional iron-oxides was attributed to interphase exchange mechanisms but neither shape nor orientation contributions were invoked for the explanation considering the relatively small deviation in the magnetic properties (M_S and K_{eff} values) of the substituted ferrites (Zn, Co, Mn) in comparison to Fe_3O_4 .

Significantly lower heating capability was obtained for doped-ferrites with mean core diameters of ca. 9 nm (i.e., in the same superparamagnetic regime as those in [22]) with a maximum of only ~100 W/g (concentration below 5 mg/mL) [25]. With regards to the improvement in SLP due to an interphase exchange mechanisms [26], an example shows synergistic effects (SLP ~500 W/g) in soft MnFe_2O_4 and hard CoFe_2O_4 bimagnetic clusters when compared with the homomagnetic 9 nm counterparts (~100 and ~200 W/g for Mn- and Co- ferrite, respectively) [27]. Such SLP values are similar to many others in the literature [28–33]. Overall, despite the superior magnetic hyperthermia response in many core-shell systems, recent experimental and theoretical studies failed to reproduce heating efficiencies above a few hundreds of watts per gram [34], in line with our observations (Table 2).

Table 2. Summary of the literature studies using magnetic core-shell nanoparticles as magnetic hyperthermia agents.

Reference	System	Size (nm)	Frequency (kHz)	SLP (W/g)
[22]	CoFe ₂ O ₄ @MnFe ₂ O ₄	15	500	2280
[23]	ZnFe ₂ O ₄ /CoFe ₂ O ₄	70	500	10,600
[24]	CoFe ₂ O ₄ @MnFe ₂ O ₄	30	500	10,810
[25]	(Zn,Co,Mn)Fe ₂ O ₄	9	850	97
[27]	MnFe ₂ O ₄ @CoFe ₂ O ₄	81	765	525
[28]	CoFe ₂ O ₄ @(Ni,Zn)Fe ₂ O ₄	10	265	25
[29]	(Zn,Co)Fe ₂ O ₄ @MnFe ₂ O ₄	11	1955	520
[30]	Fe ₃ O ₄ @(Zn,Co)Fe ₂ O ₄	9.4	817	190
[31]	CoFe ₂ O ₄ @MnFe ₂ O ₄	14.4	1950	320
[32]	CoFe ₂ O ₄ @Fe ₃ O ₄	12.8	183	59
[33]	Fe ₃ O ₄ @(Zn,Co)Fe ₂ O ₄	13	97	380
[35]	(Zn,Co)Fe ₂ O ₄ @(Zn,Mn)Fe ₂ O ₄	7.6	200	1343
[36]	(Co,Mn)Fe ₂ O ₄	15	420	1718
[37]	(Co,Mn)Fe ₂ O ₄	22	380	3417
[38]	Zn-doped Fe ₃ O ₄	40	293	1675
[39]	Fe ₃ O ₄ @(Co,Zn)Fe ₂ O ₄	18	309	2400

Still, values around 1300 W/g were claimed for Zn/Co and Zn/Mn ferrite core-shell nanocubes with mean size about 10 nm, although certain issues, such as the negative slope for water control experiment was overlooked [35]. Of note, the measured SAR values of around 1700 W/g for 15 nm hexagonal-shaped CoMn-doped iron oxides in tetrahydrofuran decreased below 1 kW/g when transferred to water through oleic acid substitution with DMSA [36]. Similarly, a heating efficiency of about 3.5 kW/g was measured for 22 nm Co-Mn doped ferrites in aqueous dispersion; however, such heating performance was due to Brownian motion, not hysteresis, and consequently decreased in high viscosity glycerol solutions that simulate cellular media [37]. These results are in agreement with those reported in cubic Co- and Zn-substituted ferrites after their cell internalization [38], where the SAR showed a reduction of about 60% in the case of Zn_{0.21}Fe_{2.79}O₄. The same tendency applies to monodisperse Fe₃O₄/Co_xZn_{1-x}Fe₂O₄ core-shell NPs [39].

Having seen the above, it is our opinion that variability of SLP values by more than three orders of magnitude, even for nominally similar samples, can mislead research in an extremely critical field of NPs application such as cancer treatment. As an approach to address these issues, the adoption of universal indices, such as the intrinsic loss power (ILP), has been proposed [40]. This is part of a standardization effort for developing validated metrology of the heating properties of NPs with the aim of obtaining interlaboratory comparable and user-independent results [41–44]. ILP manages to unify performance data but only for relatively low and slow fields and for samples that fit to the Langevin superparamagnetic regime. Otherwise, ILP values from even the same sample may vary upon field conditions [45]. Indeed, the definition of ILP assumes that hysteretic losses per cycle are frequency independent, which may not be true [46]. Additionally, it can even be confounding because, for instance, a value of ILP as high as 14 nH·m²/kg [45], corresponds to a SLP of no more than ~200 W/g, which is insufficient for clinical translation, i.e., extremely high concentration would be required to succeed conditions for cancer cells' death [47]. In any case, such “normalizing” approaches would help to establish the practical limits of what nanotechnology can deliver and identify a better way to evaluate results.

3.3. Perspectives

In our case, the simultaneous presence of the Fe and Fe₃O₄ phases provides an optimum way to combine high M_S values without the need to employ biologically incompatible elements (Mn, Co, Ni) either in the form of oxides or as alloys. Additionally, the core-shell configuration which is spontaneously achieved by the described chemistry-free method

has the potential to result in the required enhanced K_{eff} . This becomes clearer by pointing out the limitations arising by the occurrence of each phase. Commonly available iron oxide ferrofluids show SLP about 100 W/g [48], while in a few special cases experimental values exceeding 500 W/g have been reported in the literature [49], which does not seem to depend much on whether Fe_3O_4 or $\text{Fe}_3\text{O}_4/\text{CoFe}_2\text{O}_4$ core-shell NPs are employed as long as optimized M_S is achieved [50]. Figure 5 further demonstrates that SLP strongly depends on the strength of the field. However, maximum values for single Fe_3O_4 NPs seem to be confined by the correlation of the applied AC field to the coercive one. Suggestively, the effect of applied field practically ceases to occur upon overcoming the coercivity of Fe_3O_4 NPs ~ 25 kA/m. On the other hand, metallic Fe is among the most efficient nanoheaters since it combines high M_S and higher coercive field than Fe_3O_4 . Such characteristics usually feature Fe NPs with low SLP values at low field intensities but are significantly improved at higher ones as coercivity is approached (40–50 kA/m). With the purpose of illustration, an extended analysis of Fe NPs with a size ranging about 6–30 nm at 274 kHz can be found in [51]. The strong dependency of Fe NPs performance to the sample concentration and field parameters was underlined for water-based dispersions which showed SLP values in the wide range 0.2–2 kW/g [14]. As a result, the presence of the iron core contributes to the enhancement of the attainable SLP as shown in Figure 5 for core-shell samples with similar characteristics to the studied ones. More specifically, owing to the M_S elevation and the effect of exchange anisotropy, the estimated SLP_{max} for the ideal core-shell samples is almost doubled with respect to the single Fe_3O_4 NPs.

With regards to the observed superiority of ideal spherical core-shell sample in Figure 5, it should be exclusively attributed to the lower mass percentage of Fe_3O_4 constituting the particles' shell in comparison to the corresponding oxide volume ratio for the cubes. However, our experimental observations differ from the theoretical predictions and indicate the nanocubes as the best performing system (Table 1). Therefore, it seems that improvement of the K_{eff} term is a dominant SLP-defining parameter overcoming the role of the contribution of the higher M_S observed for the spherical counterparts. Furthermore, the assembling of the nanocubes in a chainlike fashion increases the correlation length, thus modifying the response to external stimuli [8,10,54]. This effect stems from the dependence of the entropy and dipolar interactions on the length of the chain, although the particular details will depend also on the chain orientation with respect to the field direction [52]. For instance, monodisperse iron-oxide NPs of 44 nm in size, assembled into chains, have achieved a heating performance of around 2 kW per Fe gram (1.5 kW/g nanoparticle) under a 24 kA/m and 765 kHz, while the same nonassembled control samples show typical iron-oxide SLP values below 500 W/g [14]. Moreover, the nanorods configuration can be considered as a particular case of the item above [53], as is also the case for magnetotactic bacteria [54] with SLP values reaching over 2 kW/g for 48 kA/m and 300 kHz.

A final mention goes to the nanoparticles' form. The deviation of nanoparticles' shapes from the isotropic (spherical) one has been often mentioned as providing a positive effect in SLP values. For instance, about 2 kW/g at 47.8 kA/m and 488 kHz were reported by Yang et al. [55] for aqueous suspensions of Fe_3O_4 nanodisks, which is perfectly consistent with calculations based on dissipation due to hysteresis loss. Similar values were also achieved with other geometries, as long as the applied fields were enough to saturate the measured samples. We mention, for example, the values reported for magnetite nanorings with an average outer diameter of 70 nm and 50 nm thickness at 96 kA/m and 400 kHz [56], and flowerlike clusters composed of 11 nm Fe_3O_4 building blocks (21.5 kA/m, 700 kHz) [57]. In this regard, we highlight the particular case of the $\text{MnFe}_2\text{O}_4/\text{Fe}_3\text{O}_4$ binary system consisting of large 34 nm MnFe_2O_4 NPs surrounded by smaller 8 nm Fe_3O_4 particles, leading to 1700 W/g at 24 kA/m and 765 kHz [58]. Further examples above 1.5 kW/g include laboratory-scale optimized NPs at 31 kA/m and 700 kHz [59] and even commercially available ones (Sigma-Aldrich 900,042 produced by Ocean Nanotec, LLC, San Diego) at 59 kA/m and 345 kHz [60].

4. Materials and Methods

4.1. Nanoparticles Preparation

Examining the role of the minimum surface-to-volume ratio appearing in spheres or the higher surface magnetic anisotropy of cubes in the determination of SLP was the motivation to compare spherical and cubic NPs in this study. Spherical core-shell Fe/Fe₃O₄ NPs were prepared using solar physical vapor deposition (SPVD) in a medium-vacuum glass chamber [61]. Such process has been conducted in the facilities of PROMES in Odeillo-Font Romeu, France. The solar furnace setup consists of a mobile plane mirror reflecting the radiation on a 2-kW parabolic concentrator (2 m diameter) and then onto the target. In our case, pressurized Fe (99.99%) powder pellets were used. The evaporation pressure was set to 70 Torr by regulating the Ar flow. Powders were collected on a nanoporous ceramic filter placed in the pumping line. A production rate of around 100 mg/h was established during these experiments though the method is capable to provide up to 10 times higher yields [62]. Spontaneous surface oxidation of Fe NPs upon exposure to air resulted in the formation of a thin iron oxide coating.

The corresponding cubic-shaped core-shell NPs were fabricated in Barcelona, Spain, using a home-built 1-in. diameter DC magnetron cluster source operating at 30 W in the low 10⁻³ Torr range. Deposition took place at a production rate of 1 mg/h using a (Fe 99.95%) target-to-substrate (corning glass) distance of 25 cm with Ar flow regulated at around 80 cm³/min in a modification of the process reported previously [8,63]. It is envisaged that given the effective high temperature near the target surface, the crystallinity could also be increased, resulting in a cubic shape vs. the lower temperature synthesis of spherical NPs by SPVD.

4.2. Characterization

The identification of the major crystalline phases was performed by X-ray diffraction (XRD) using a Rigaku UltimaPlus operating at 40 kV and 30 mA with CuK α radiation, step size 0.05° and step time 2 s. Obtained diagrams were evaluated after comparison to the Powder Diffraction Files (PDF) database [64]. The size and morphological characteristics of the NPs were studied by means of transmission electron microscopy (TEM) using a JEM-1210 (JEOL) microscope, operating at 120 kV. TEM samples were prepared by depositing a drop of the particles' water dispersion onto a carbon coated copper grid. The size of around 100 NPs was determined to estimate the size distribution, the average particles dimensions and the standard deviation for each sample, i.e., the average variability from the mean value corresponding to the diameter for spherical NPs and the side for cubic ones. Sample weighting was performed in a 4-digit analytical balance with an error of ± 0.1 mg.

Magnetic characterization was carried out in a superconducting quantum interference device (SQUID) Quantum Design MPMS XL-7T magnetometer by measuring the magnetization-applied field diagrams. Hysteresis loops corresponding to fields beyond saturation (4 T) and minor loops in the range of magnetic hyperthermia (24–48 kA/m) were recorded at 300 K.

Heating efficiency under magnetic hyperthermia conditions was evaluated through calorimetric measurements using a 1.2-kW Ambrell Easyheat 0112 AC field generator operating at 375 kHz and magnetic field intensities up to 48 kA/m. Used coil providing an homogeneous field, consisted of 8 turns with a total height of 4.5 cm and an inner diameter of around 2.5 cm. Temperature was monitored during the experiment using an Opsens PicoM device with a GaAs-based fiber optic probe immersed in the center of a cylindrical vessel (inner diameter 1 cm) containing 1 mL of dispersion. Dispersions of the studied NPs are generally kept stable in distilled water for around 1 h and such behavior was preserved even months after their preparation, indicating no tendency for nonreversible aggregation during storage.

Although this study aims to a fundamental description of the impact on magneto-heating response, the selected working conditions comply with the recently revisited limit threshold for safe clinical use without patient discomfort (2×10^9 A / m s) [65]. Nanopar-

ticles were dispersed in water to prepare a stable suspension of 1 mg/mL after bubbling with nitrogen to displace dissolved oxygen and so minimize oxidation or hydrolysis effects. In order to rule out interfering contributions, the SLP was estimated by the slope of the temperature versus time curve after subtracting the signal from water control samples and heat losses to the environment [43] as:

$$\text{SLP} = C_p \frac{m_f}{m_n} \cdot \frac{\Delta T}{\Delta t} \quad (1)$$

where C_p is the specific heat of the solution, m_f the solution mass, m_n the mass of nanoparticles and $\Delta T/\Delta t$ the initial slope of the heating curve.

4.3. Theoretical Estimations

The aforementioned calorimetric measurements are usually performed under nonadiabatic conditions, which require data analysis to remove potential error sources. Hence, it is best complemented with results from AC magnetometry and/or quantification of magnetic losses by theoretical considerations. In order to estimate theoretically the maximum achievable efficiency within the given field conditions, the following approach was applied. Let us first presume that we have a group of identical particles (assuming no size distribution) whose response to an applied field is linear to a very high frequency, which, for iron and its oxides under common hyperthermia conditions, is expected to occur for particles of few tens of nanometers in size. The maximum amount of electromagnetic energy (E_{\max}) that could be absorbed per cycle of magnetic field $H_{AC} = H_{app} \cdot \sin(2\pi ft)$, where f is the field frequency and H_{app} the amplitude, corresponds to that of a square hysteresis loop [66]:

$$E_{\max} = 2H_{app} \cdot 2\mu_0 M_S V \quad (2)$$

with μ_0 being the permeability of the free space. Thus, optimizing the hyperthermia performance implies reaching the closer possible to this theoretical limit.

It is evident that ellipsoidal-type hysteresis loops as those described by the Linear Response Theory are far from this behaviour; on the contrary, it readily comes from uniaxial-symmetry monodomain crystals if the magnetic field is applied parallel to the easy axis direction [67] under condition $H_{app} = 2K_{eff}/\mu_0 M_S$, i.e., with the field amplitude matching that of the particles' anisotropy field. In that case Equation (2) can be rewritten as:

$$E_{\max} = 8K_{eff} \cdot V \quad (3)$$

and therefore, the maximum SLP is given by:

$$\text{SLP}_{\max} = 4 \frac{\mu_0}{\rho} M_S \cdot H_{app} \cdot f \quad (4)$$

It is obvious that by just introducing the M_S values from the hysteresis loops, the applied field amplitude and frequency, and the average density estimated by the weighted average of Fe/Fe₃O₄ in each system, it was possible to obtain SLP_{\max} .

One should note that such maximum heating performance is theoretically defined by basic electromagnetic considerations in terms of field and particle-magnetization properties, regardless of the actual anisotropy of the particles. Optimizing the released heat is, thus, equivalent to finding the optimum magnetization (M_S)-anisotropy (K_{eff}) combination, a goal that researchers have usually searched for by tuning particle shape [68] or composition [69]. While both approaches have proven in general very successful, both suffer from limitations. In this regard, core-shell compositions based on iron and its oxides offer a robust way to overcome most of these limitations, as we have previously shown [6]; here we aim to put together the core-shell approach with the shape contribution to the magnetic and heating properties for systems with similar volumes and core-to-shell ratios.

It is important to mention that the above stands for the ideal theoretical conditions, and any deviation from this arrangement will bring a decreased SLP. For instance, either

the nonperfect alignment of the field and easy axis, dipole–dipole interactions or thermal activation, modify the hysteresis shape. Thus, it is usually suggested that a particle system will be randomly distributed within a viscous biological medium; in this case, a quick estimate using the Stoner–Wohlfarth model indicates that (for noninteracting conditions) the remanence and coercivity are half of the M_S and anisotropy field, respectively. Then, Equation (3) shall be reduced by four (other proportionality factors would apply whether the magnetization switching is controlled by, for instance, a cubic magnetocrystalline anisotropy) [70,71]. As a last note, this is valid only if the external field matches the coercive field (H_C), otherwise the system is likely to be subjected to nonsaturating magnetic fields and will therefore be cycled around minor hysteresis loops with consequently smaller heat release (on the other hand, even if $H_{app} > H_C$ then the losses would be limited to $4 \frac{\mu_0}{\rho} M_S H_C \cdot f$).

5. Conclusions

The amount of energy transferred per unit time and mass of magnetic material during the application of an AC magnetic field has been the subject of enormous studies pointing to the potential use in biomedical practices, but only recently have we begun to understand this. Herein, cubic- and spherical-shaped Fe/Fe₃O₄ core-shell NPs developed by chemistry-free evaporation methods are shown to possess most of the required features for the amelioration of magnetic hyperthermia efficiencies, i.e., high M_S , exchange effects, shape anisotropy, and chain formation. The used approach is one of the few methods to obtain the specific Fe/Fe₃O₄ core-shell nanoparticles with similar total and shell dimensions in two different shapes, in the quest to understand the shape effect with real experimentally obtained samples. Nonetheless, the results showed that the obtained SLP values lie 2–3 orders of magnitude below the expected ones for ideal systems. In addition, the anisotropy enhancement in cubic NPs appears as a more crucial contribution to establish a higher SLP in spite of the higher M_S in spherical ones. In summary, the presented data support the prospect of increasing the heating efficiency, although SLP values above tens of kW/g ferrofluid at affordable magnetic fields seem to be just out of reach. Future work will demonstrate if this hypothesis holds true.

Supplementary Materials: The following are available at <https://www.mdpi.com/article/10.3390/magnetochemistry7040049/s1>.

Author Contributions: Conceptualization, C.M.-B.; methodology, K.S. and D.S.; data curation, L.B., J.O. and A.M.; writing—original draft preparation, C.M.-B., K.S. and D.S.; writing—review and editing, C.M.-B., K.S. and D.S.; visualization, K.S. All authors have read and agreed to the published version of the manuscript.

Funding: We thank the CNRS-PROMES laboratory, UPR 8521, belonging to the French National Centre for Scientific Research (CNRS) for providing access to its installations, the support of its scientific and technical staff (N. Bouillet, E. Guillot, A. Badziaka), and the financial support of the SFERA-III project (Grant Agreement No 823802). Spanish Ministry of Science, Innovation and Universities through grant (CEX2019-000917-S) in the framework of the Spanish Severo Ochoa Centre of Excellence Program and RTI2018-099960-B-I00 (SPINCURIOX). This research is cofinanced by Greece and the European Union (European Social Fund-ESF) through the Operational Programme “Human Resources Development, Education and Lifelong Learning” in the context of the project “Reinforcement of Postdoctoral Researchers—2nd Cycle” (MIS-5033021), implemented by the State Scholarships Foundation (IKY).

Data Availability Statement: Please refer to suggested Data Availability Statements in section “MDPI Research Data Policies” at <https://www.mdpi.com/ethics>.

Conflicts of Interest: The authors declare no conflict of interest.

References

1. Kok, H.P.; Cressman, E.N.K.; Ceelen, W.; Brace, C.L.; Ivkov, R.; Gröll, H.; ter Haar, G.; Wust, P.; Crezee, J. Heating technology for malignant tumors: A review. *Int. J. Hypertherm.* **2020**, *37*, 711–741. [[CrossRef](#)]

2. Gilchrist, R.K.; Medal, R.; Shorey, W.D.; Hanselman, R.C.; Parrot, J.C.; Taylor, C.B. Selective inductive heating of lymph nodes. *Ann. Surg.* **1957**, *146*, 596–606. [[CrossRef](#)] [[PubMed](#)]
3. Etemadi, H.; Plieger, P.G. Magnetic Fluid Hyperthermia Based on Magnetic Nanoparticles: Physical Characteristics, Historical Perspective, Clinical Trials, Technological Challenges, and Recent Advances. *Adv. Ther.* **2020**, *3*, 2000061. [[CrossRef](#)]
4. Conde-Leboran, I.; Baldomir, D.; Martinez-Boubeta, C.; Chubykalo-Fesenko, O.; Del Puerto Morales, M.; Salas, G.; Cabrera, D.; Camarero, J.; Teran, F.J.; Serantes, D. A Single Picture Explains Diversity of Hyperthermia Response of Magnetic Nanoparticles. *J. Phys. Chem. C* **2015**, *119*, 15698–15706. [[CrossRef](#)]
5. Tong, S.; Zhu, H.; Bao, G. Magnetic iron oxide nanoparticles for disease detection and therapy. *Mater. Today* **2019**, *31*, 86–99. [[CrossRef](#)]
6. Simeonidis, K.; Martinez-Boubeta, C.; Serantes, D.; Ruta, S.; Chubykalo-Fesenko, O.; Chantrell, R.; Oró-Solé, J.; Balcells, L.; Kamzin, A.S.; Nazipov, R.A.; et al. Controlling Magnetization Reversal and Hyperthermia Efficiency in Core-Shell Iron-Iron Oxide Magnetic Nanoparticles by Tuning the Interphase Coupling. *ACS Appl. Nano Mater.* **2020**, *3*, 4465–4476. [[CrossRef](#)] [[PubMed](#)]
7. Liu, J.; Su, D.; Wu, K.; Wang, J.P. High-moment magnetic nanoparticles. *J. Nanoparticle Res.* **2020**, *22*, 1–16. [[CrossRef](#)]
8. Balcells, L.; Stanković, I.; Konstantinović, Z.; Alagh, A.; Fuentes, V.; López-Mir, L.; Oró, J.; Mestres, N.; García, C.; Pomar, A.; et al. Spontaneous in-flight assembly of magnetic nanoparticles into macroscopic chains. *Nanoscale* **2019**, *11*, 14194–14202. [[CrossRef](#)]
9. Serantes, D.; Baldomir, D.; Martinez-Boubeta, C.; Simeonidis, K.; Angelakeris, M.; Natividad, E.; Castro, M.; Mediano, A.; Chen, D.X.; Sanchez, A.; et al. Influence of dipolar interactions on hyperthermia properties of ferromagnetic particles. *J. Appl. Phys.* **2010**, *108*, 073918. [[CrossRef](#)]
10. Martinez-Boubeta, C.; Simeonidis, K.; Makridis, A.; Angelakeris, M.; Iglesias, O.; Guardia, P.; Cabot, A.; Yedra, L.; Estradé, S.; Peiró, F.; et al. Learning from Nature to Improve the Heat Generation of Iron-Oxide Nanoparticles for Magnetic Hyperthermia Applications. *Sci. Rep.* **2013**, *3*, 1652. [[CrossRef](#)]
11. Tong, S.; Quinto, C.A.; Zhang, L.; Mohindra, P.; Bao, G. Size-Dependent Heating of Magnetic Iron Oxide Nanoparticles. *ACS Nano* **2017**, *11*, 6808–6816. [[CrossRef](#)]
12. Davis, H.C.; Kang, S.; Lee, J.H.; Shin, T.H.; Putterman, H.; Cheon, J.; Shapiro, M.G. Nanoscale Heat Transfer from Magnetic Nanoparticles and Ferritin in an Alternating Magnetic Field. *Biophys. J.* **2020**, *118*, 1502–1510. [[CrossRef](#)] [[PubMed](#)]
13. Martinez-Boubeta, C.; Simeonidis, K.; Serantes, D.; Conde-Leborán, I.; Kazakis, I.; Stefanou, G.; Peña, L.; Galceran, R.; Balcells, L.; Monty, C.; et al. Adjustable hyperthermia response of self-assembled ferromagnetic Fe-MgO core-shell nanoparticles by tuning dipole-dipole interactions. *Adv. Funct. Mater.* **2012**. [[CrossRef](#)]
14. Serantes, D.; Simeonidis, K.; Angelakeris, M.; Chubykalo-Fesenko, O.; Marciello, M.; Del Puerto Morales, M.; Baldomir, D.; Martinez-Boubeta, C. Multiplying magnetic hyperthermia response by nanoparticle assembling. *J. Phys. Chem. C* **2014**, *118*, 5927–5934. [[CrossRef](#)]
15. Bondarenko, A.V.; Holmgren, E.; Li, Z.W.; Ivanov, B.A.; Korenivski, V. Chaotic dynamics in spin-vortex pairs. *Phys. Rev. B* **2019**, *99*. [[CrossRef](#)]
16. Snoeck, E.; Gatel, C.; Lacroix, L.M.; Blon, T.; Lachaize, S.; Carrey, J.; Respaud, M.; Chaudret, B. Magnetic configurations of 30 nm iron nanocubes studied by electron holography. *Nano Lett.* **2008**, *8*, 4293–4298. [[CrossRef](#)]
17. López-Conesa, L.; Martínez-Boubeta, C.; Serantes, D.; Estradé, S.; Peiró, F. Mapping the Magnetic Coupling of Self-Assembled Fe₃O₄ Nanocubes by Electron Holography. *Materials* **2021**, *14*, 774. [[CrossRef](#)]
18. Usov, N.A.; Nesmeyanov, M.S.; Tarasov, V.P. Magnetic vortices as efficient nano heaters in magnetic nanoparticle hyperthermia. *Sci. Rep.* **2018**, *8*. [[CrossRef](#)]
19. McClurg, G.O. Magnetic Field Distributions for a Sphere and for an Ellipsoid. *Am. J. Phys.* **1956**, *24*, 496–499. [[CrossRef](#)]
20. Munoz-Menendez, C.; Conde-Leboran, I.; Serantes, D.; Chantrell, R.; Chubykalo-Fesenko, O.; Baldomir, D. Distinguishing between heating power and hyperthermic cell-treatment efficacy in magnetic fluid hyperthermia. *Soft Matter* **2016**, *12*, 8815–8818. [[CrossRef](#)]
21. Munoz-Menendez, C.; Serantes, D.; Ruso, J.M.; Baldomir, D. Towards improved magnetic fluid hyperthermia: Major-loops to diminish variations in local heating. *Phys. Chem. Chem. Phys.* **2017**, *19*, 14527–14532. [[CrossRef](#)] [[PubMed](#)]
22. Lee, J.-H.; Jang, J.-T.; Choi, J.-S.; Moon, S.H.; Noh, S.-H.; Kim, J.-W.; Kim, J.-G.; Kim, I.-S.; Park, K.I.; Cheon, J. Exchange-coupled magnetic nanoparticles for efficient heat induction. *Nat. Nanotechnol.* **2011**, *6*, 418–422. [[CrossRef](#)] [[PubMed](#)]
23. Noh, S.H.; Na, W.; Jang, J.T.; Lee, J.H.; Lee, E.J.; Moon, S.H.; Lim, Y.; Shin, J.S.; Cheon, J. Nanoscale magnetism control via surface and exchange anisotropy for optimized ferrimagnetic hysteresis. *Nano Lett.* **2012**, *12*, 3716–3721. [[CrossRef](#)] [[PubMed](#)]
24. Moon, S.H.; Noh, S.H.; Lee, J.H.; Shin, T.H.; Lim, Y.; Cheon, J. Ultrathin Interface Regime of Core-Shell Magnetic Nanoparticles for Effective Magnetism Tailoring. *Nano Lett.* **2017**, *17*, 800–804. [[CrossRef](#)]
25. Pardo, A.; Pelaz, B.; Gallo, J.; Bañobre-López, M.; Parak, W.J.; Barbosa, S.; Del Pino, P.; Taboada, P. Synthesis, Characterization, and Evaluation of Superparamagnetic Doped Ferrites as Potential Therapeutic Nanotools. *Chem. Mater.* **2020**, *32*, 2220–2231. [[CrossRef](#)]
26. Lavorato, G.C.; Das, R.; Alonso Masa, J.; Phan, M.-H.; Srikanth, H. Hybrid magnetic nanoparticles as efficient nanoheaters in biomedical applications. *Nanoscale Adv.* **2021**. [[CrossRef](#)]
27. Vamvakidis, K.; Mourdikoudis, S.; Makridis, A.; Paulidou, E.; Angelakeris, M.; Dendrinou-Samara, C. Magnetic hyperthermia efficiency and MRI contrast sensitivity of colloidal soft/hard ferrite nanoclusters. *J. Colloid Interface Sci.* **2018**, *511*, 101–109. [[CrossRef](#)]

28. Phadatare, M.R.; Meshram, J.V.; Gurav, K.V.; Kim, J.H.; Pawar, S.H. Enhancement of specific absorption rate by exchange coupling of the core-shell structure of magnetic nanoparticles for magnetic hyperthermia. *J. Phys. D Appl. Phys.* **2016**, *49*. [[CrossRef](#)]
29. Hammad, M.; Nica, V.; Hempelmann, R. Synthesis and Characterization of Bi-Magnetic Core/Shell Nanoparticles for Hyperthermia Applications. *IEEE Trans. Magn.* **2017**, *53*. [[CrossRef](#)]
30. Fabris, F.; Lima, E.; De Biasi, E.; Troiani, H.E.; Vásquez Mansilla, M.; Torres, T.E.; Fernández Pacheco, R.; Ibarra, M.R.; Goya, G.F.; Zysler, R.D.; et al. Controlling the dominant magnetic relaxation mechanisms for magnetic hyperthermia in bimagnetic core-shell nanoparticles. *Nanoscale* **2019**, *11*, 3164–3172. [[CrossRef](#)]
31. Nica, V.; Caro, C.; Páez-Muñoz, J.M.; Leal, M.P.; Garcia-Martin, M.L. Bi-magnetic core-shell CoFe₂O₄@MnFe₂O₄ nanoparticles for in vivo theranostics. *Nanomaterials* **2020**, *10*, 907. [[CrossRef](#)]
32. Sanna Angotzi, M.; Mamelì, V.; Cara, C.; Musinu, A.; Sangregorio, C.; Niznansky, D.; Xin, H.L.; Vejpravova, J.; Cannas, C. Coupled hard-soft spinel ferrite-based core-shell nanoarchitectures: Magnetic properties and heating abilities. *Nanoscale Adv.* **2020**, *2*, 3191–3201. [[CrossRef](#)]
33. Darwish, M.S.A.; Kim, H.; Lee, H.; Ryu, C.; Lee, J.Y.; Yoon, J. Engineering core-shell structures of magnetic ferrite nanoparticles for high hyperthermia performance. *Nanomaterials* **2020**, *10*, 991. [[CrossRef](#)] [[PubMed](#)]
34. Carrião, M.S.; Bakuzis, A.F. Mean-field and linear regime approach to magnetic hyperthermia of core-shell nanoparticles: Can tiny nanostructures fight cancer? *Nanoscale* **2016**, *8*, 8363–8377. [[CrossRef](#)]
35. Wang, L.; Yan, Y.; Wang, M.; Yang, H.; Zhou, Z.; Peng, C.; Yang, S. An integrated nanoplatfrom for theranostics via multifunctional core-shell ferrite nanocubes. *J. Mater. Chem. B* **2016**, *4*, 1908–1914. [[CrossRef](#)] [[PubMed](#)]
36. Albarqi, H.A.; Wong, L.H.; Schumann, C.; Sabei, F.Y.; Korzun, T.; Li, X.; Hansen, M.N.; Dhagat, P.; Moses, A.S.; Taratula, O.; et al. Biocompatible Nanoclusters with High Heating Efficiency for Systemically Delivered Magnetic Hyperthermia. *ACS Nano* **2019**, *13*, 6383–6395. [[CrossRef](#)] [[PubMed](#)]
37. He, S.; Zhang, H.; Liu, Y.; Sun, F.; Yu, X.; Li, X.; Zhang, L.; Wang, L.; Mao, K.; Wang, G.; et al. Maximizing Specific Loss Power for Magnetic Hyperthermia by Hard–Soft Mixed Ferrites. *Small* **2018**, *14*. [[CrossRef](#)]
38. Pardo, A.; Yáñez, S.; Piñero, Y.; Iglesias-Rey, R.; Al-Modlej, A.; Barbosa, S.; Rivas, J.; Taboada, P. Cubic Anisotropic Co- And Zn-Substituted Ferrite Nanoparticles as Multimodal Magnetic Agents. *ACS Appl. Mater. Interfaces* **2020**, *12*, 9017–9031. [[CrossRef](#)]
39. Lavorato, G.C.; Das, R.; Xing, Y.; Robles, J.; Litterst, F.J.; Baggio-Saitovitch, E.; Phan, M.H.; Srikanth, H. Origin and Shell-Driven Optimization of the Heating Power in Core/Shell Bimagnetic Nanoparticles. *ACS Appl. Nano Mater.* **2020**, *3*, 1755–1765. [[CrossRef](#)]
40. Kallumadil, M.; Tada, M.; Nakagawa, T.; Abe, M.; Southern, P.; Pankhurst, Q.A. Suitability of commercial colloids for magnetic hyperthermia. *J. Magn. Magn. Mater.* **2009**, *321*, 1509–1513. [[CrossRef](#)]
41. Makridis, A.; Curto, S.; Van Rhooon, G.C.; Samaras, T.; Angelakeris, M. A standardisation protocol for accurate evaluation of specific loss power in magnetic hyperthermia. *J. Phys. D Appl. Phys.* **2019**, *52*, 255001. [[CrossRef](#)]
42. Asimakidou, T.; Makridis, A.; Veintemillas-Verdaguer, S.; Morales, M.P.; Kellartzis, I.; Mitrakas, M.; Vourlias, G.; Angelakeris, M.; Simeonidis, K. Continuous production of magnetic iron oxide nanocrystals by oxidative precipitation. *Chem. Eng. J.* **2020**, *393*, 124593. [[CrossRef](#)]
43. Chalkidou, A.; Simeonidis, K.; Angelakeris, M.; Samaras, T.; Martinez-Boubeta, C.; Balcells, L.; Papazisis, K.; Dendrinou-Samara, C.; Kalogirou, O. In vitro application of Fe/MgO nanoparticles as magnetically mediated hyperthermia agents for cancer treatment. *J. Magn. Magn. Mater.* **2011**, *323*, 775–780. [[CrossRef](#)]
44. Rubia-Rodríguez, I.; Santana-Otero, A.; Spassov, S.; Tombácz, E.; Johansson, C.; De La Presa, P.; Teran, F.J.; Morales, M.D.P.; Veintemillas-Verdaguer, S.; Thanh, N.T.K.; et al. Whither magnetic hyperthermia? A tentative roadmap. *Materials* **2021**, *14*, 706. [[CrossRef](#)] [[PubMed](#)]
45. Lanier, O.L.; Korotych, O.I.; Monsalve, A.G.; Wable, D.; Savliwala, S.; Grooms, N.W.F.; Nacea, C.; Tuitt, O.R.; Dobson, J. Evaluation of magnetic nanoparticles for magnetic fluid hyperthermia. *Int. J. Hyperth.* **2019**, *36*, 687–701. [[CrossRef](#)] [[PubMed](#)]
46. Rao, M.; Krishnamurthy, H.R.; Pandit, R. Magnetic hysteresis in two model spin systems. *Phys. Rev. B* **1990**, *42*. [[CrossRef](#)] [[PubMed](#)]
47. Hergt, R.; Dutz, S. Magnetic particle hyperthermia-biophysical limitations of a visionary tumour therapy. *J. Magn. Magn. Mater.* **2007**, *311*, 187–192. [[CrossRef](#)]
48. Bakoglidis, K.D.; Simeonidis, K.; Sakellari, D.; Stefanou, G.; Angelakeris, M. Size-dependent mechanisms in AC magnetic hyperthermia response of iron-oxide nanoparticles. *IEEE Trans. Magn.* **2012**, *48*, 1320–1323. [[CrossRef](#)]
49. Hergt, R.; Hiergeist, R.; Hilger, I.; Kaiser, W.A.; Lapatnikov, Y.; Margel, S.; Richter, U. Maghemite nanoparticles with very high AC-losses for application in RF-magnetic hyperthermia. *J. Magn. Magn. Mater.* **2004**, *270*, 345–357. [[CrossRef](#)]
50. Robles, J.; Das, R.; Glassell, M.; Phan, M.H.; Srikanth, H. Exchange-coupled Fe₃O₄/CoFe₂O₄ nanoparticles for advanced magnetic hyperthermia. *AIP Adv.* **2018**, *8*. [[CrossRef](#)]
51. Mehdaoui, B.; Meffre, A.; Carrey, J.; Lachaize, S.; Lacroix, L.M.; Gougeon, M.; Chaudret, B.; Respaud, M. Optimal size of nanoparticles for magnetic hyperthermia: A combined theoretical and experimental study. *Adv. Funct. Mater.* **2011**, *21*, 4573–4581. [[CrossRef](#)]
52. Torche, P.; Munoz-Menendez, C.; Serantes, D.; Baldomir, D.; Livesey, K.L.; Chubykalo-Fesenko, O.; Ruta, S.; Chantrell, R.; Hovorka, O. Thermodynamics of interacting magnetic nanoparticles. *Phys. Rev. B* **2020**, *101*, 224429. [[CrossRef](#)]

53. Das, R.; Alonso, J.; Nematı Porshokouh, Z.; Kalappattıl, V.; Torres, D.; Phan, M.H.; Garaio, E.; García, J.Á.; Sanchez Llamazares, J.L.; Srikanth, H. Tunable High Aspect Ratio Iron Oxide Nanorods for Enhanced Hyperthermia. *J. Phys. Chem. C* **2016**, *120*, 10086–10093. [[CrossRef](#)]
54. Gandia, D.; Gandarias, L.; Rodrigo, I.; Robles-García, J.; Das, R.; Garaio, E.; García, J.Á.; Phan, M.H.; Srikanth, H.; Orue, I.; et al. Unlocking the Potential of Magnetotactic Bacteria as Magnetic Hyperthermia Agents. *Small* **2019**, *15*. [[CrossRef](#)]
55. Yang, Y.; Liu, X.; Lv, Y.; Herng, T.S.; Xu, X.; Xia, W.; Zhang, T.; Fang, J.; Xiao, W.; Ding, J. Orientation mediated enhancement on magnetic hyperthermia of Fe₃O₄ nanodisc. *Adv. Funct. Mater.* **2015**, *25*, 812–820. [[CrossRef](#)]
56. Liu, X.L.; Yang, Y.; Ng, C.T.; Zhao, L.Y.; Zhang, Y.; Bay, B.H.; Fan, H.M.; Ding, J. Magnetic Vortex Nanorings: A New Class of Hyperthermia Agent for Highly Efficient in Vivo Regression of Tumors. *Adv. Mater.* **2015**, *27*, 1939–1944. [[CrossRef](#)] [[PubMed](#)]
57. Hugounenq, P.; Levy, M.; Alloyeau, D.; Lartigue, L.; Dubois, E.; Cabuil, V.; Ricolleau, C.; Roux, S.; Wilhelm, C.; Gazeau, F.; et al. Iron oxide monocrystalline nanoflowers for highly efficient magnetic hyperthermia. *J. Phys. Chem. C* **2012**, *116*, 15702–15712. [[CrossRef](#)]
58. Simeonidis, K.; Viñas, S.L.; Wiedwald, U.; Ma, Z.; Li, Z.-A.; Spasova, M.; Patsia, O.; Myrovali, E.; Makridis, A.; Sakellari, D.; et al. A versatile large-scale and green process for synthesizing magnetic nanoparticles with tunable magnetic hyperthermia features. *RSC Adv.* **2016**, 53107–53117. [[CrossRef](#)]
59. Fortin, J.-P.; Wilhelm, C.; Servais, J.; Ménager, C.; Bacri, J.-C.; Gazeau, F. Size-sorted anionic iron oxide nanomagnets as colloidal mediators for magnetic hyperthermia. *J. Am. Chem. Soc.* **2007**, *129*, 2628–2635. [[CrossRef](#)]
60. Lanier, O.L.; Monsalve, A.G.; McFetridge, P.S.; Dobson, J. Magnetically triggered release of biologics. *Int. Mater. Rev.* **2019**, *64*, 63–90. [[CrossRef](#)]
61. Simeonidis, K.; Martínez-Boubeta, C.; Balcells, L.; Monty, C.; Stavropoulos, G.; Mitrakas, M.; Matsakidou, A.; Vourlias, G.; Angelakeris, M. Fe-based nanoparticles as tunable magnetic particle hyperthermia agents. *J. Appl. Phys.* **2013**, *114*. [[CrossRef](#)]
62. Martínez-Boubeta, C.; Simeonidis, K.; Amarantidis, S.; Angelakeris, M.; Balcells, L.; Monty, C. Scaling up the production of magnetic nanoparticles for biomedical applications: Cost-effective fabrication from basalts. *Phys. Status Solidi Curr. Top. Solid State Phys.* **2014**, *11*, 1053–1058. [[CrossRef](#)]
63. Balcells, L.; Martínez-Boubeta, C.; Cisneros-Fernández, J.; Simeonidis, K.; Bozzo, B.; Oró-Sole, J.; Bagués, N.; Arbiol, J.; Mestres, N.; Martínez, B. One-Step Route to Iron Oxide Hollow Nanocuboids by Cluster Condensation: Implementation in Water Remediation Technology. *ACS Appl. Mater. Interfaces* **2016**, *8*, 28599–28606. [[CrossRef](#)] [[PubMed](#)]
64. Joint Center for Powder Diffraction Studies (Ed.) *Powder Diffraction File*, 2004th ed.; International Centre for Diffraction Data: Newtown Square, PA, USA, 2004.
65. Bellizzi, G.; Bucci, O.M.; Chirico, G. Numerical assessment of a criterion for the optimal choice of the operative conditions in magnetic nanoparticle hyperthermia on a realistic model of the human head. *Int. J. Hyperth.* **2016**, *32*, 688–703. [[CrossRef](#)]
66. Dennis, C.L.; Krycka, K.L.; Borchers, J.A.; Desautels, R.D.; Van Lierop, J.; Huls, N.F.; Jackson, A.J.; Gruettner, C.; Ivkov, R. Internal Magnetic Structure of Nanoparticles Dominates Time-Dependent Relaxation Processes in a Magnetic Field. *Adv. Funct. Mater.* **2015**, *25*, 4300–4311. [[CrossRef](#)]
67. Conde-Leborán, I.; Serantes, D.; Baldomir, D. Orientation of the magnetization easy axes of interacting nanoparticles: Influence on the hyperthermia properties. *J. Magn. Magn. Mater.* **2015**, *380*, 321–324. [[CrossRef](#)]
68. Arciniegas, M.P.; Castelli, A.; Brescia, R.; Serantes, D.; Ruta, S.; Hovorka, O.; Satoh, A.; Chantrell, R.; Pellegrino, T. Unveiling the Dynamical Assembly of Magnetic Nanocrystal Zig-Zag Chains via In Situ TEM Imaging in Liquid. *Small* **2020**, *16*. [[CrossRef](#)]
69. Balakrishnan, P.B.; Silvestri, N.; Fernandez-Cabada, T.; Marinaro, F.; Fernandes, S.; Fiorito, S.; Miscuglio, M.; Serantes, D.; Ruta, S.; Livesey, K.; et al. Exploiting Unique Alignment of Cobalt Ferrite Nanoparticles, Mild Hyperthermia, and Controlled Intrinsic Cobalt Toxicity for Cancer Therapy. *Adv. Mater.* **2020**, *32*. [[CrossRef](#)]
70. García-Otero, J.; Porto, M.; Rivas, J.; Bunde, A. Influence of the cubic anisotropy constants on the hysteresis loops of single-domain particles: A Monte Carlo study. *J. Appl. Phys.* **1999**, *85*, 2287–2292. [[CrossRef](#)]
71. Johnson, C.E.; Brown, W.F. Stoner-Wohlfarth Calculation on Particle with Both Magnetocrystalline and Shape Anisotropy. *J. Appl. Phys.* **1959**, *30*, S320–S322. [[CrossRef](#)]